Protocol-independent granular temperature supported by numerical simulations

Volker Becker* and Klaus Kassner†

Institute for Theoretical Physics, Otto von Guericke University Magdeburg, Postfach 4120, D-39106 Magdeburg, Germany

(Received 31 May 2015; revised manuscript received 27 August 2015; published 5 November 2015)

A possible approach to the statistical description of granular assemblies starts from Edwards's assumption that all blocked states occupying the same volume are equally probable [Edwards and Oakeshott, Physica A **157**, 1080 (1989)]. We performed computer simulations using two-dimensional polygonal particles excited periodically according to two different protocols: excitation by pulses of "negative gravity" and excitation by "rotating gravity." The first protocol exhibits a nonmonotonous dependency of the mean volume fraction on the pulse strength. The overlapping histogram method is used in order to test whether the volume distribution is described by a Boltzmann-like distribution and to calculate the inverse compactivity as well as the logarithm of the partition sum. We find that the mean volume is a unique function of the measured granular temperature, independently of the protocol and of the branch in $\phi(g)$, and that all determined quantities are in agreement with Edwards's theory.

DOI: 10.1103/PhysRevE.92.052201 PACS number(s): 45.70.−n, 05.20.Gg

I. INTRODUCTION

Granular materials are typically composed of thousands to millions of individual particles (or more). Think, for example, of the cereals for breakfast or of the sand on the shore. These large numbers suggest that statistical methods may be applicable and constitute a powerful tool in developing a better theoretical understanding of these kinds of materials. However, contrary to the situation in gases or fluids, where the permitted phase space is explored continuously due to chaotic molecular motion, thermal fluctuations are negligible for granular materials. Furthermore, the particle dynamics are dissipative. Therefore, it is not possible to carry standard statistical mechanics over to granular assemblies. In particular, the classical Boltzmann distribution, where the probability of a state is inversely proportional to the exponential of its energy (measured in units of $k_B T$), will not apply to these systems.

Edwards and Oakeshott [1,2] proposed that concepts from classical statistical mechanics are applicable if one assumes that the volume of a static, stable granulate plays the same role in granular statistics as the energy of a microstate in classical statistics. This means that, analogously to the classical microcanonical ensemble, where all states with the same energy are equally probable, all mechanically stable configurations of the granular assembly that occupy the same volume occur with the same probability. The entropy of this granular microcanonical ensemble is proportional to the logarithm of the number of blocked states with a certain volume. By analogy with classical statistics, one can define a temperature-like variable, called compactivity, as the inverse of the derivative of the Edwards entropy with respect to the volume. Later, it turned out that for a full description of a granular system, beyond the volume ensemble also an ensemble for the different stress states must be introduced [3–5] and that the volume and the stress ensembles are probably interdependent [6]. However, it seems that expectation values of quantities that depend on the geometrical state only and not on the stress state are well described by the volume ensemble [7], possibly because the force-moment tensor can be treated as approximately constant in the systems considered here. Therefore we focus on the volume ensemble in most of the present paper.

Some doubts about the temperature-like interpretation of the compactivity have been raised on the basis of equilibration experiments performed by Puckett and Daniels [8]. They found that in a two-component system, the compactivity did not equilibrate, whereas the angoricity did. There are different ways to explain this observation, some of which do not necessitate to give up the interpretation of the compactivity as a temperature-like variable [9].

A key assumption of standard statistical mechanics is the equivalence of time and ensemble averages, but mechanically stable granular configurations are static states without any intrinsic time evolution. On the other hand, by applying the same external excitation to the granular material again and again (i.e., tapping [10] or shearing [11]), this external excitation may take over the role of thermal agitation and the concept of a time average becomes meaningful for granular statistics as well. Some tests of the ergodicity of granular systems are available in the literature. With systems of frictional disks excited with flow pulses, equivalence between time and ensemble averages was found [12]. In the case of a vertical tapping protocol, dependency on the protocol parameters was noted. Especially for small tapping amplitudes, nonergodicity was observed in numerical simulations [13]. This may be related to the occurrence of irreversible branches in tapped granular systems [10,14].

As a cautionary remark we note that athermal granular aggregates may be in mechanical equilibrium but are typically in thermodynamically nonequilibrium states. Edwards's approach should not be misinterpreted as somehow turning a nonequilibrium system into an equilibrium one. Pragmatically, Edwards suggests a maximization principle to hold for a quantity conveniently called entropy (by analogy with a similar quantity in statistical mechanics), given certain side conditions (e.g., constant mean volume in the granular analog of the canonical ensemble). While for most nonequilibrium systems no extremum principles are available, there are a few even in classical statistical mechanics admitting a description

*Volker.Becker@ovgu.de
†Klaus.Kassner@ovgu.de

via such a principle. Steady-state systems not too far from equilibrium are governed by a principle of minimum entropy production, and pattern-forming systems near a bifurcation (i.e., a nonequilibrium phase transition) may in some cases be described by a variational equation (the real Ginzburg-Landau equation), derivable from minimization of a functional. When such a principle can be applied, it greatly simplifies the characterization of the nonequilibrium system. The utility of Edwards's approach is to motivate, and to provide us with, a maximum principle for a particular kind of nonequilibrium systems. Its applicability does not rely on equilibrium in the thermodynamic sense, even though the analogy from which it derives introduces a language similar to that used in the statistical physics of equilibrium systems. It also suggests that certain "equilibration" procedures may be used to generate the desired nonequilibrium ensemble. However, equilibration is not with respect to temperature but with respect to compactivity, a variable characterizing a nonequilibrium state in a similar way as an order parameter (analogous to a magnetization) may characterize a nonequilibrium phase in a pattern-forming system.

Several methods were proposed to determine the compactivity from experimental or simulation data [10,15–17] and applied to different kinds of granulates. In this work, we employ two-dimensional discrete-element (DEM) simulations using polygonal particles to apply two different excitation protocols to otherwise identical granulates. This allows us to determine whether the calculated compactivity is independent of the specific excitation protocol (which would support the Edwards theory) or not (which would oppose it). Recently, some authors have addressed the issue of whether it is necessary to introduce protocol-specific extensions of Edwards-like approaches [18,19]. We briefly discuss a possible approach in Sec. II B. At least for the two protocols considered in this paper, we find protocol independence. Furthermore, we test whether ideal-gas-like prediction analogies of the Edwards theory are consistent with the simulation data and find good qualitative agreement, which even becomes quantitative if certain parameters are chosen by fitting.

The paper is organized as follows. In Sec. II, we give an overview of some aspects of Edwards's theory, relevant to this work. In Sec. III, we introduce the simulation technique. Section IV gives details of the applied excitation protocols and, in Sec. V, the simulation results will be presented, evaluated, and discussed. In Sec. VI, some limitations of the volume ensemble are illustrated. Finally, Sec. VII gives a summary of our findings.

II. THEORETICAL FRAMEWORK

A. The microcanonical and the canonical volume ensemble

The main assumption of the Edwards theory is the following [1,2]: If a granular ensemble is generated by a *reproducible* preparation protocol, all resulting mechanically stable configurations of the granular system which occupy the same volume will occur with the same probability on repetition of the protocol. This means that in Edwards's granular statistics the volume plays the same role as the energy in ordinary statistics. Consequently, the entropy S of the microcanonical ensemble having a certain volume V is given as the logarithm of the number Ω of stable states (in the permitted phase space) occupying this volume.

Let a microstate of the granular ensemble, comprised of N particles, be described by a set of variables $\boldsymbol{q}$. The entropy of this state is given by (see, e.g., Refs. [1,2,7]):

$$S(V,N) = \ln \Omega(V,N), \tag{1}$$

$$\Omega(V,N) = \int_{\{\boldsymbol{q}\}} d\boldsymbol{q}\, \delta[V - W(\boldsymbol{q})]. \tag{2}$$

The integral runs over all stable configurations $\{\boldsymbol{q}\}$ and the function $W(\boldsymbol{q})$ gives the volume of the state $\boldsymbol{q}$. Note that in this context, $W(\boldsymbol{q})$ is the granular analog of the Hamiltonian and V is the analog of the internal energy.

By analogy with standard statistical mechanics, an intensive, temperature-like variable χ can be defined, usually called compactivity:

$$\chi = \beta^{-1} = \frac{\partial V}{\partial S}. \tag{3}$$

In this paper, we will, for simplicity, mostly use the "thermodynamic beta," defined as the inverse compactivity $\beta = 1/\chi$, instead of the compactivity itself.

Note that, in general, a constant λ analogous to the Boltzmann constant may be introduced in Eqs. (1) and (3). Here we use $\lambda = 1$, which means that we measure compactivity in units of volume.

As in ordinary statistics and thermodynamics (see, e.g., Ref. [20]) one may switch from the microcanonical ensemble to the canonical ensemble by a Legendre transformation. In the corresponding canonical ensemble, the probability of a microstate $\boldsymbol{q}$ occupying the volume $W(\boldsymbol{q})$ is given by a Boltzmann-like distribution:

$$P(\boldsymbol{q}) = \frac{1}{Z} e^{-\beta W(\boldsymbol{q})} \tag{4}$$

with the canonical partition function [6,17,21]

$$Z = \int_{\{q\}} d\boldsymbol{q}\, e^{-\beta W(\boldsymbol{q})}. \tag{5}$$

Once again, the integral runs over all possible mechanically stable states. Note that this is equivalent to a notation often used in the literature, where the integral runs over all states and contains an additional factor $\theta(\boldsymbol{q})$, which takes the value zero for forbidden states and one for allowed ones, thus selecting the permitted states.

Note that a tapping protocol does not necessarily lead to canonical sampling of the system. A trivial example would be tapping with so small an amplitude that the system is trapped in the initial blocked state. A nontrivial example is the irreversible branch for vertical tapping observed by Nowak *et al.* [10]. Also, the comparison between the analytically solvable Bowles-Ashwin model system [22] and simulations where such a system is vertically tapped [23] exhibits deviations from the canonical ensemble prediction. Note that the Bowles-Ashwin model assumes a highly confined geometry with much lower complexity than realistic granular systems. Vertical tapping applied to this special system with strong confinement may be unsuited for phase space exploration

according to a flat probability measure. Or else the flat Edwards measure does not hold in general. Even if that were the case, a meaningful definition of compactivity might still be possible as will be described now.

B. Generalized (protocol dependent) ensembles

In case it turned out that Edwards's assumption of a flat probability measure is not satisfied for the microcanical ensemble, it is possible to modify the ensemble with (in general, state and protocol dependent) weighting factors $w(\boldsymbol{q})$ [3,18,19]. The microcanical state density would be modified as follows:

$$\Omega_G(V,N) = \int_{\{\boldsymbol{q}\}} d\boldsymbol{q}\, w(\boldsymbol{q}) \delta[V - W(\boldsymbol{q})]. \tag{6}$$

Providing we have

$$\Omega_G(V_1 + V_2, N) = \Omega_G(V_1, N_1)\, \Omega_G(V_2, N_2), \tag{7}$$

which is a much weaker assumption than a flat probability measure [3], it is still possible to define a compactivity. The canonical formulation for the volume ensemble then reads

$$P(\boldsymbol{q}) = w(\boldsymbol{q}) \frac{1}{Z} e^{-\beta W(\boldsymbol{q})}, \tag{8}$$

$$Z_G = \int_{\{q\}} d\boldsymbol{q}\, w(\boldsymbol{q}) e^{-\beta W(\boldsymbol{q})}. \tag{9}$$

A similar approach is feasible for the force-moment and the combined ensembles. Generalized canonical ensembles of this kind are used in statistical genetics [24,25].

The qualitative impact of these modifications on the resulting thermodynamics is small. Especially Eqs. (17) and (20) remain unaffected, as long as the weighting factors are the same for all data samples. If only one protocol is used, then it is impossible to detect protocol dependencies in the weighting factors. But a comparison of different protocols, applied to the same system, may help to decide whether these factors, if their introduction should turn out necessary, are protocol independent.

C. Mean volume and volume fluctuations

The calculation of the mean volume and its fluctuations is straightforward. The first derivative of the logarithm of (5) [or (9)] with respect to β essentially is the mean volume

$$\langle V \rangle = -\frac{\partial}{\partial \beta} \ln Z = \frac{1}{Z} \int_{\{q\}} d\boldsymbol{q}\, W(\boldsymbol{q}) e^{-\beta W(\boldsymbol{q})}, \tag{10}$$

whereas its second derivative is the variance of the volume distribution, i.e., a measure for the strength of fluctuations.

$$\sigma_V^2 = \langle V^2 \rangle - \langle V \rangle^2 = \frac{\partial^2}{\partial \beta^2} \ln Z, \tag{11}$$

$$\sigma_V^2 = -\frac{\partial}{\partial \beta} \langle V \rangle. \tag{12}$$

Instead of the volume itself, we use the volume fraction ϕ, defined as the sum of the grain volumes V_g divided by the volume W occupied by the granulate:

$$\phi(\boldsymbol{q}) = \frac{V_g}{W(\boldsymbol{q})}. \tag{13}$$

The volume $W(\boldsymbol{q})$ of a certain state can be written as a sum of the mean volume $V = \langle W \rangle$ and the deviation from the mean: $W = V + \Delta V$. Under the assumption that the volume fluctuations are small compared to the mean volume, we can write:

$$\phi = \frac{V_g}{V + \Delta V} \simeq \frac{V_g}{V} - \frac{V_g}{V^2} \Delta V. \tag{14}$$

The mean volume fraction is therefore:

$$\bar{\phi} = \langle \phi \rangle = \frac{V_g}{V}, \tag{15}$$

and from Eqs. (14) and (15), together with $\langle \Delta V^2 \rangle = \sigma_V^2$, we obtain

$$\sigma_\phi^2 = \langle (\phi - \bar{\phi})^2 \rangle = \frac{\langle \phi \rangle^4}{V_g^2} \sigma_V^2. \tag{16}$$

Substituting σ_V^2 from Eq. (12) and reexpressing the differential of $\langle V \rangle$ according to $d\langle V \rangle = -V_g / \langle V \rangle^2 d\bar{\phi}$, we find a relation between the mean volume fraction and its fluctuations:

$$\sigma_\phi^2 = \frac{\bar{\phi}^2}{V_g} \frac{\partial \bar{\phi}}{\partial \beta}. \tag{17}$$

Measuring the volume fraction fluctuations as a function of the mean volume fraction and integrating Eqs. (17) or (12), respectively, is a way to calculate the compactivity up to an unknown constant. It is used frequently, e.g., in Refs. [10,15,17]. Note that determining the granular temperature via Eqs. (12) or (17) is just a rule of calculation, provided by Edwards's theory but no proof of the theory. On the other hand, if after determining β in some different way the relationship (17) linking it with the volume fraction were not satisfied, a contradiction to Edwards's theory would have been demonstrated.

D. Overlapping histogram method

Another way to determine the inverse compactivity is the overlapping histogram method proposed in 2003 by Dean and Lefèvre [26]. This method may also be used as a test of whether a distribution of blocked states is Boltzmann-like distributed. In the original paper, the method was applied to the energy of the Sherrington-Kirkpatrick model for spin glasses, driven by a tappinglike mechanism, which has some similarities to granular dynamics. The method was then frequently used to determine the granular temperature [8,17,27,28]. Under the assumption that Edwards's theory holds, the probability to measure a certain volume V in a granulate with an inverse compactivity β_0 and a fixed number of grains N is

$$\begin{aligned} P(V,\beta_0,N) &= \int_{\{\boldsymbol{q}\}} d\boldsymbol{q}\, \delta[V - W(\boldsymbol{q})] \frac{1}{Z(\beta_0,N)} e^{-\beta_0 W(\boldsymbol{q})} \\ &= \frac{\mathfrak{D}(V,N)}{Z(\beta_0,N)} e^{-\beta_0 V}, \end{aligned} \tag{18}$$

where $\mathfrak{D}(V,N)$ is the number of blocked states with volume V, i.e., $\mathfrak{D}(V,N) = \Omega(V,N)$. This equation holds even for

the generalized nonflat probability measure approach, when Eq. (6) is used for $\Omega(V,N)$.

We define the quantity Q as the logarithm of the ratio of probability densities for the volume V to arise, on the one hand, at an inverse compactivity β_1 and, on the other hand, in a reference system held at a different inverse compactivity β_0:

$$Q := \ln \frac{P(V,\beta_1,N)}{P(V,\beta_0,N)}, \tag{19}$$

$$Q = \underbrace{(\beta_0 - \beta_1)}_{:=A_{10}} V + \underbrace{\ln \frac{Z(\beta_0,N)}{Z(\beta_1,N)}}_{:=B_{10}}. \tag{20}$$

Therefore, if we measure the probability density $P(V,\beta,N)$ for different compactivities and calculate $Q(V)$, the resulting function must be linear if Edwards's theory holds. Evaluating the slope A_{10} allows us to determine the inverse compactivity up to an additive constant. Furthermore, the intercept B_{10} is nothing else than the logarithm of the partition function up to an additive constant at the corresponding inverse compactivity. This permits testing the validity of Edwards's assumption in the sense that if $Q(V)$ were not a straight line, then neither Eq. (4) nor Eq. (8) would describe the probability density of the system correctly.

However, one has to be somewhat careful with the interpretation of the results, as has been pointed out in Ref. [27]. Under certain circumstances, very similar results as the ones expected from Edwards's theory can occur if the distributions of the samples are just Gaussian. In Appendix A, we discuss this situation.

E. Ideal quadron solution

There are very few real *ab initio* predictions from Edwards's theory in the literature [6,21,29,30], due to some general difficulties. In order to calculate analytical expressions for the partition function, knowledge of an explicit expression for the granular Hamiltonian $W(\boldsymbol{q})$ is necessary. Of course, if all positions, orientations and shapes of the grains are known, the occupied volume is a function of these quantities, but in practice it is not easy to write down an explicit equation and even if this can be done, the integration over the permitted blocked states is very difficult because the permitted states are unknown in general.

Therefore, attempts to calculate the partition function were based on standard volume tessellations, such as the Voronoi and Delaunay tessellations [30–33]. A possible alternative is an arch-based approach [34] which *a priori* takes only stable configurations into account. Blumenfeld and Edwards proposed a physically motivated tessellation based on the quadron construction [5,7,29,35]. In principle, quadrons are used as quasiparticles describing the structure of the granulate at any arbitrary position within the system in a distinct way. It was mentioned in the literature that the ideal quadron tesselation fails in the presence of nonconvex voids in the granulate [36]. However, in a system of monodisperse spheres such nonconvex voids vanish by neglecting rattlers [37]. Even if some nonconvex voids remain, they could be tesselated by convex polygons which repairs the quadron tessellation, at the price that the number of quadrons increases. As long as nonconvex voids are the exception rather than the rule, they will not produce significant changes to the calculations.

Under the (very rough) assumption that quadrons occupy volumes between $V_0 - \Delta$ and $V_0 + \Delta$ at constant density of states and that there are no interactions between the quadrons, the partition function can be calculated explicitly for two-dimensional systems (see Ref. [29]):

$$Z = \left[\frac{\sinh(\beta\Delta)}{\beta\Delta} e^{-\beta V_0} \right]^{N\bar{z}}, \tag{21}$$

where N is the number of particles and $\bar{z}$ is the mean coordination number in the granular system. This approximation is called the ideal quadron approximation by analogy with the description of ideal gases in ordinary statistics. Note that the partition function (21) is a special version of a more general ideal-gas-like approach. If one assumes that the volume is tesselated by a number $\tilde{N}$ of statistically independent, noninteracting elementary cells and their volume is restricted to an interval between a minimal volume $V_0 - \Delta$ and a maximal volume $V_0 + \Delta$, without any additional assumption on the nature of these elementary cells one ends up with Eq. (21), on replacing $N\bar{z} \to \tilde{N}$. Contrary to the very general ideal-gas-like approach, there are some possibilities to go beyond the interaction-free situation in the quadron approach, which will be considered in future work.

Using (10), the ideal quadron prediction for the mean volume is obtained:

$$\langle V \rangle = N\bar{z} \left[V_0 + \frac{1}{\beta} - \Delta \coth(\beta\Delta) \right]. \tag{22}$$

For the current work, it is helpful to rewrite (22) in terms of the volume fraction. Dividing (22) by the total grain volume V_g results in

$$\bar{\phi}^{-1} = \frac{N\bar{z}V_0}{V_g} + \frac{N\bar{z}}{V_g\beta} - \frac{N\bar{z}\Delta}{V_g} \coth(\beta\Delta). \tag{23}$$

In order to specify the free parameters V_0 and Δ, we assume that the limits of $\bar{\phi}^{-1}$ can be identified with the volume fractions of random loose packing (rlp) and random close packing (rcp) in the following way:

$$\phi_{\mathrm{rlp}}^{-1} = \lim_{\beta\to 0} \bar{\phi}^{-1} = \frac{N\bar{z}V_0}{V_g}, \tag{24}$$

$$\phi_{\mathrm{rcp}}^{-1} = \lim_{\beta\to \infty} \bar{\phi}^{-1} = \frac{N\bar{z}(V_0 - \Delta)}{V_g}. \tag{25}$$

Now we can rewrite (23) as

$$\bar{\phi}^{-1} = \phi_{\mathrm{rlp}}^{-1} + \frac{N\bar{z}}{V_g\beta} - \Delta_\phi^{-1} \coth\left(\beta \frac{V_g \Delta_\phi^{-1}}{N\bar{z}} \right), \tag{26}$$

where $\Delta_\phi^{-1} = \phi_{\mathrm{rlp}}^{-1} - \phi_{\mathrm{rcp}}^{-1}$. Below, Eq. (26) will be useful as a fitting function for our simulation data.

We remark that the ideal quadron solution is a very rough estimation, because the main difficulty in the calculation of the partition function (5) is filtering out stable configurations. In the ideal quadron solution, a minimal filtering is performed in the sense that there is a minimal and a maximal volume per quadron so configurations that are either too loose or too dense are filtered out. However, the number of states between these

limits may be overestimated. The arch-based approach [34] may have the capability to overcome this issue. However, in the current form no analytical equation such as (26) is available. Only numerical solutions under very simplifying assumptions are on hand, which makes a comparison of our data with this model difficult.

Note that there is no commonly accepted definition of the states rlp and rcp. In this paper we use these terms in the sense of Eqs. (24) and (25). An interesting fact is that in the framework of the ideal quadron model for $\beta \to 0$, which is the limit of very high compactivities, the mean volume per quadron is V_0, not $V_0 + \Delta$. States which would have a mean volume per quadron with $\bar{V} > V_0$ correspond to a population inversion, i.e., states with negative granular temperature. It may be speculated that these states correlate with so-called random very loose packings states [38], which are states only achievable with very special protocols. A verification of this idea is beyond the scope of the present article.

III. SIMULATION METHOD

In our simulation, we extend an existing DEM code, originally developed for the investigation of the mechanical properties of granular piles consisting of two-dimensional polygonal particles [39,40]. While the two-dimensionality is certainly a restriction of our code, its implementation of polygonal particles constitutes a gain in realism over simulations using circular disks. The dynamics of the ith particle's position $\boldsymbol{r}_i$ and orientation ϕ_i are described by Newton's and Euler's equations of motion:

$$m_i \ddot{\boldsymbol{r}}_i = \sum_{j \neq i} \boldsymbol{F}_{ij} + \boldsymbol{F}_i^V, \tag{27}$$

$$J_i \ddot{\phi}_i = \sum_{j \neq i} M_{ij}. \tag{28}$$

Herein, $\boldsymbol{F}_{ij}$ is the contact force between particle i and particle j, M_{ij} is the corresponding torque acting on the particle (referred to its center of mass), and $\boldsymbol{F}_i^V$ is the external force acting on the particle (e.g., gravity). The mass of particle i is denoted by m_i and its moment of inertia by J_i [41–43]. We assume external torques to be absent.

For fast determination of potential particle contacts, the particles are surrounded by bounding boxes and we employ an incremental sort-and-update algorithm [39,40] to identify overlapping bounding boxes efficiently. Whenever the bounding boxes of two particles overlap, we use a closest-feature algorithm [39,40] from virtual reality and robotics applications [44] to calculate the polygon distance. In the worst-case scenario, the computational complexity is $\mathcal{O}(n \log n)$, where n is the number of polygon features (corners and edges). However, the typical behavior, whenever a good guess from the last time step is available, is the calculation of the polygon distance in constant time $\mathcal{O}(1)$, independently of the polygon edge number.

Figure 1 shows a sketch of two particles in contact. The contact point s_{ij} between two particles is defined as the midpoint of the line between c_1 and c_2. For the force calculation, we define some quantities first: the characteristic

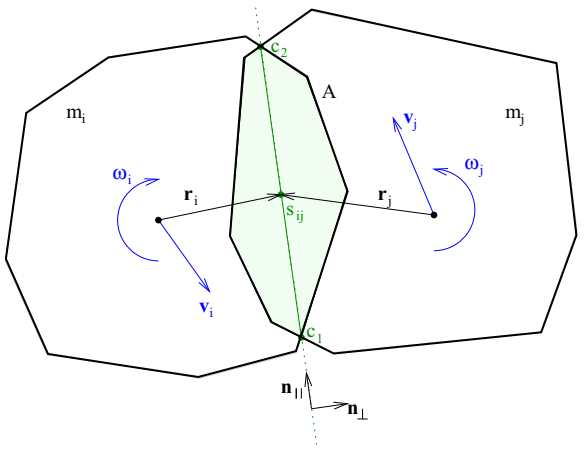

FIG. 1. (Color online) Sketch of two polygonal particles in contact. The normal and tangential direction of a collision is determined by the contact line (green); the contact point is defined as the middle of the contact line.

length

$$l = \frac{r_i r_j}{r_i + r_j} \tag{29}$$

(note that l is not the length of the contact line), the reduced mass

$$m_\perp = \frac{m_i m_j}{m_i + m_j}, \tag{30}$$

and the reduced tangential mass, including the moments of inertia,

$$m_\parallel = \frac{1}{\frac{1}{m_i} + \frac{1}{m_j} + \frac{r_i^2}{J_i} + \frac{r_j^2}{J_j}}. \tag{31}$$

The relative tangential velocity at the contact point s_{ij} is

$$v_\parallel = [\boldsymbol{v}_i - \boldsymbol{v}_j + (\boldsymbol{r}_i \times \boldsymbol{\omega}_i) - (\boldsymbol{r}_j \times \boldsymbol{\omega}_j)] \cdot \boldsymbol{n}_\parallel, \tag{32}$$

where $\boldsymbol{v}_i, \boldsymbol{v}_j$ are the velocities of the particles and $\boldsymbol{\omega}_i, \boldsymbol{\omega}_j$ are their angular velocities. Furthermore, we define the effective penetration length as

$$h_{\text{eff}} = \frac{A}{l}. \tag{33}$$

Note that l does not change significantly during a collision, so h_{eff} is essentially proportional to the overlap area A. The normal component of the contact force is determined by the equation

$$F_\perp = \max[E h_{\text{eff}} - \gamma \sqrt{E m_\perp} \dot{h}_{\text{eff}}; 0]. \tag{34}$$

Here E is the two-dimensional Young's modulus and γ is the dissipation strength.

The maximum function in Eq. (34) ensures that the normal force cannot become attractive. Physically, situations where the dissipative term overcomes the repulsive force correspond to the case that the particles' separation velocity is faster than the relaxation velocity of the grain deformation, i.e., the contact between the particles is lost, before the overlap of the nondeformable model particles becomes zero [45].

Consequently, the contact force vanishes from this moment onward.

We used the Cundall-Strack model [46] for modeling tangential forces. At the beginning of the collision, the Cundall-Strack force F^* is zero. If this force is given at the previous time step, corresponding to time $t_c - \Delta t$, then the Cundall-Strack force at the current time step at time t_c is determined by

$$F_\parallel^*(t_c) = \min\left[F_\parallel^*(t_c-\Delta t)+v_\parallel(t_c-\Delta t)\Delta t\tfrac{2}{7}E;\mu F_\perp(t_c)\right]. \tag{35}$$

One may visualize this model as a spring between the contact points being established when a new contact appears and the length of the spring being limited by the value of Coloumb friction (Coulomb condition). If this value is reached, then the points of attachment of the spring start to slide, so the spring length remains constant. In this way, the Cundall-Strack model mimics sticking and sliding friction. In order to avoid unrealistic oscillations, a damping term proportional to the velocity is added to the Cundall-Strack force, which also satisfies the Coloumb conditions. The complete trangential force then is

$$F_\parallel(t_c) = \min\left[F_\parallel^*(t_c) + v_\parallel\sqrt{\frac{2}{7}Em_\parallel};\mu F_\perp(t_c)\right]. \tag{36}$$

With (34) and (36), all the contact forces and the resulting torques between the particles and between particles and walls (which are treated as particles with fixed position and orientation) are defined. The equations of motion (27) and (28) are then solved numerically using a sixth-order Gear predictor-corrector method [47].

IV. EXCITATION PROTOCOLS AND PARAMETERS

Inspired by former experimental studies [15–17], we implemented two protocols for exciting the granular matter periodically. In both protocols, an excitation period in which the phase space is explored alternates with a relaxation period in which the grains come to rest completely. Both protocols are characterized by a control parameter, which we call the tapping parameter.

In all simulations, we used a bidisperse mixture of 1184 regular decagons, composed of 544 particles with radius $r_1 = 9$ mm and 640 particles with radius $r_2 = 6.36$ mm. Young's modulus was set to $E = 1000$ N/m and the simulation time step was chosen as $\Delta t = 5 \times 10^{-5}$ s. The Coulomb friction coefficent was taken to be $\mu = 0.6$ and for the normal friction coefficent $\gamma = 0.5$ was used. The particles mass density was $\rho = 0.001$ g/mm^2 and was the same for big and small particles.

With both protocols, the width of the simulation area was 480 mm. In the case of the negative-g protocol, there is no lid, for the rotating-g protocol the height of the box is 900 mm. Walls are realized as fixed rectangular particles with the same Young's modulus and friction coefficients as the mobile particles.

Tejada *et al.* [48] pointed out that the size of the time step in DEM simulations may influence the width and the shape (but not the mean) of the determined probability distributions, even if the time step appears sufficiently small using common criteria. In order to make sure that this effect does not influence our results, we repeated some of the simulations with a time step of $\Delta t = 10^{-5}$ s. We found that the mean volume fraction, the volume fraction variance and also the shape of the volume fraction distribution did not change on reduction of the time step.

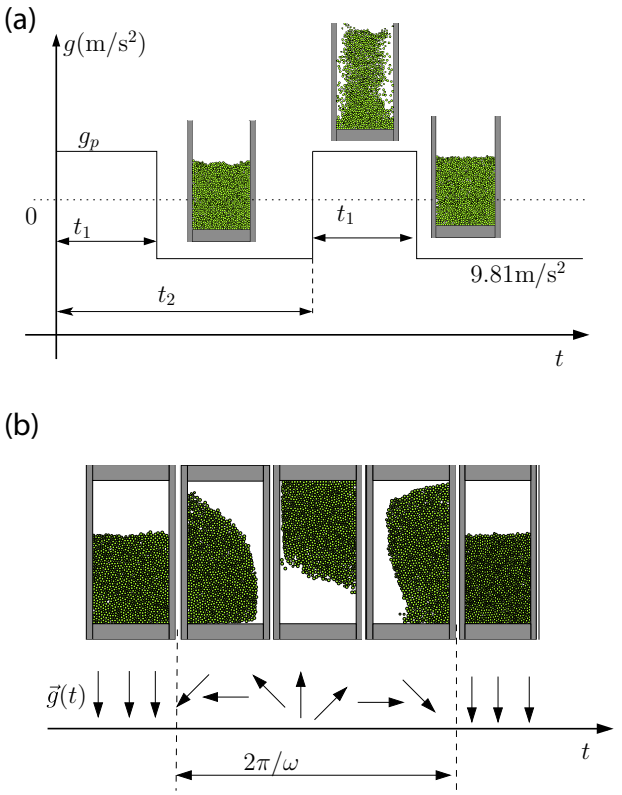

FIG. 2. (Color online) (a) The "negative-g" protocol: For a short time interval t_1 the gravity is turned upward with a prescribed magnitude. Afterwards, the granular system has time to come to rest completely, before the next pulse starts. (b) The "rotating-g" protocol: The gravitational acceleration vector performs a complete rotation. Afterwards, the granular system comes to rest completely before the next round starts.

The first protocol, called "pulses of negative gravitation" or "negative-g" protocol, is illustrated in Fig. 2(a). Most of the time, the granulate is at rest in a container under normal gravitation, but for short time intervals, the direction of gravitational acceleration is reversed. The time dependence of the gravitational acceleration $g(t)$ is taken to be

$$\boldsymbol{g}(t) = 9.81\ \mathrm{m/s^2}\boldsymbol{e}_y \times \begin{cases} g_p & \tilde{t} < t_1 \\ -1 & \text{otherwise} \end{cases}. \tag{37}$$

Here $\tilde{t} = t \bmod T$ is the simulation time t modulus the period T of the protocol and t_1 is the duration of a pulse. We took the pulse length to be $t_1 = 0.1$ s and the period $T = 3$ s. The relaxation period was chosen so that for the biggest excitation amplitudes the resulting volume fraction variations due to remaining kinetic energy in the system are smaller than 10^{-5} which is 100 times smaller than the typical magnitude of the observed static volume fraction fluctuations.

The pulse amplitude g_p was used as a tapping parameter. Due to Einstein's equivalence principle, this protocol is equivalent, per period, to a downward acceleration $(g_p + 1)g$ for an interval t_1 and a subsequent stoppage in the gravitational field for a time span $T - t_1$, taken long enough for the granulate to come to rest. Here and in the following when we write g, we mean $g = 9.81\ \mathrm{m/s^2}$.

Figure 2(b) illustrates the second protocol. The granulate is at rest in a closed box. Then the gravitational acceleration performs a complete rotation followed by a relaxation period:

$$\boldsymbol{g}(t) = 9.81\ \mathrm{m/s^2} \times \begin{cases} \sin(\omega t)\boldsymbol{e}_x - \cos(\omega t)\boldsymbol{e}_y & \tilde{t} < \frac{\omega}{2\pi} \\ -\boldsymbol{e}_y & \text{otherwise} \end{cases}. \tag{38}$$

As in the negative-g case, $\tilde{t} = t \bmod T$ is the simulation time t modulus the period T. The angular frequency ω is the control parameter of the protocol. Of course, $T > 2\pi/\omega$ must be fulfilled. In our simulations, we used $T = 2\pi/\omega + 3$ s, with $\omega \gtrsim 4\ \mathrm{s^{-1}}$. For both protocols, we tested whether segregation of the particles occurs by measuring the cumulative number of small and big grains as function of the column height $n(h)$ (i.e., the number of small or big particles with z coordinates smaller than h). These curves are straight lines and do not change during the simulations, except for fluctuations. Therefore we conclude that in our simulations segregation did not take place.

V. DETERMINATION OF COMPACTIVITY, FLUCTUATIONS AND THE PARTITION FUNCTION

For both protocols and each choice of the tapping parameter the simulations ran for 2500–3000 excitation and relaxation periods. Note that this relatively high number of taps is necessary to draw serious conclusions for the systems used here. While the confidence interval of the mean volume fraction became sufficiently small after some hundred taps, this was not the case for the estimated variance. In test simulations, where only a few hundred taps were considered, the uncertainty of the estimated variance [[49], pp. 771–772] was as big as the domain of the measured variance itself.

Immediately before the relaxation period ended, we determined the volume fraction of the granulate by measuring the fraction of solid particles in a test volume. The test volume shown in Fig. 3 is a square with edge length of 400 mm and was chosen in such a way that some layers of particles were between the borders of the test region and the walls.

It was pointed out [50] that test volumes must be big enough to avoid size-dependent effects. To make sure that our test volume is sufficiently large, we divided it into two neighboring columns. The relative difference of mean volume fraction (after 2500 taps) between the columns and the entire test volume was always smaller than 0.01% and the deviation of the volume fraction fluctuation ratio from $\sqrt{2}$ was always lower than 1%.

Figure 4 shows some typical time series for both protocols. The mean volume fraction reaches a steady-state value very quickly (after approximately <10 taps) and then only fluctuations around its mean value occur.

In Fig. 5, the mean value of the volume fraction $\bar{\phi}$ and the standard deviation of the volume fraction distribution,

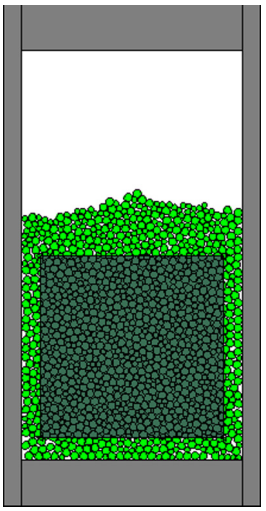

FIG. 3. (Color online) A typical situation when the granulate is at rest. The region shaded gray is the test volume, used for volume fraction determination.

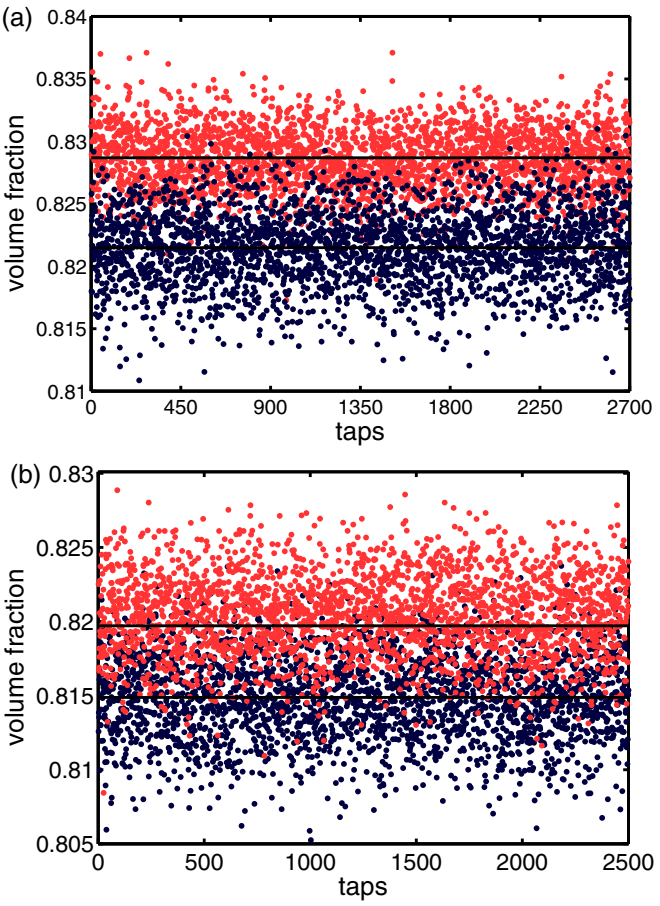

FIG. 4. (Color online) Exemplary time series for both protocols. The points are the volume fractions calculated from simulation data and the solid lines are the corresponding mean values. The tapping parameter is for the "negative-g" protocol (a): $g_p g = 6\ \mathrm{m/s^2}$ (red or gray points) and $g_p g = 28\ \mathrm{m/s^2}$ (blue or dark gray points) and for the "rotating-g" protocol $\omega = 0.75 \times 2\pi\ \mathrm{s^{-1}}$ (red or gray points) and $\omega = 2 \times 2\pi\ \mathrm{s^{-1}}$ (blue or dark gray points).

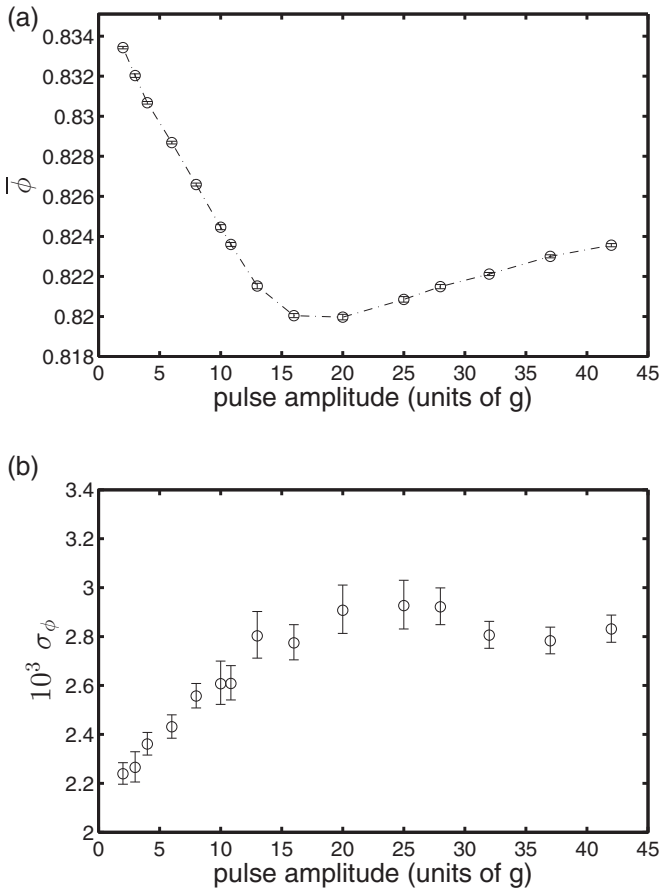

FIG. 5. Simulation results for the "negative-g" protocol: (a) the mean volume fraction as function of the pulse strength in units of earth acceleration is depicted and (b) shows the standard deviation of the volume fraction fluctuations. The error bars correspond to a confidence interval of 95%.

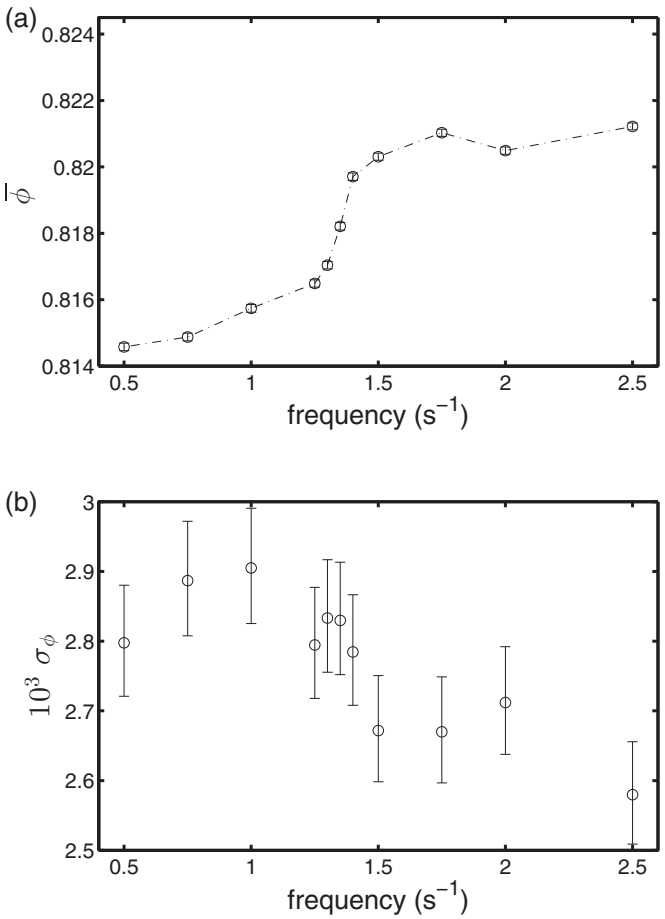

FIG. 6. Simulation results for the "rotating-g" protocol: Part (a) shows the mean volume fraction as function of rotation frequency $f = \omega/(2\pi)$ and (b) shows the standard derivation of the volume fraction fluctuations. The error bars correspond to a confidence interval of 95%.

characterizing the volume fraction fluctuation strength, are shown. Initially, the volume fraction decreases with increasing pulse strength until it reaches a local minimum around $g_p = 20$. Afterwards, the volume fraction increases with the pulse strength. Similar behavior for tapped granulates at high tapping strengths was described in Refs. [51,52]. A possible explanation is the interplay between two competing effects. First, the stronger the pulse of negative gravitation, the more the granulate is whirled around, i.e., the looser the resulting packing should get. On the other hand, the stronger the pulse, the higher the granulate flies, therefore the higher its impact velocity when it reaches the bottom, resulting in stronger compaction during the relaxation period. The first effect dominates for relatively small values of g_p, the second effect becomes more important for stronger pulses. At the same value of g_p, where the volume fraction is minimal, the volume fraction *fluctuations* have a local maximum [see Fig. 5(b)]. Similar results were found in work by Pugnaloni *et al.* [52].

The corresponding results for the "rotating-g" protocol are shown in Fig. 6. With increasing frequency the mean volume fraction shows a crossover from $\bar{\phi} \simeq 0.814$ to $\bar{\phi} \simeq 0.821$. When the frequency is very small, a complete rotation takes a long time and the granulate behaves in a quasistatic way. It is clear that in this case a further decrease of the frequency will not have a significant influence on the resulting volume fraction. Therefore, for small frequencies the $\phi(\omega)$ curve should approach a plateau. When the frequency increases, the rotation gets faster, the granulate is more strongly whirled around and becomes looser. When the frequency increases further, the time per rotation gets smaller which compensates the increase of swirling due to faster rotation. For very high frequency, one expects that the system reaches an irreversible regime, because it does not have time to respond to the rotation pulse and will largely stay in the initial configuration—but this regime is not reached in our simulations.

In order to determine the granular temperature of the samples with the overlapping histogram method, the probability density distribution of the volume fraction must be estimated. Notwithstanding the name of the approach, we used the more sophisticated kernel density estimation method [53,54] instead of histograms in order to obtain an approximation for the probability density. A normal kernel was employed and the bandwidth was chosen according to Silverman's rule of thumb [55]. In Appendix B, a short description of the approach is offered.

Some of the determined probability density distributions are shown in Fig. 7(a) for the "negative-g" protocol and in Fig. 8(a) for the "rotating-g" protocol. In order to test if

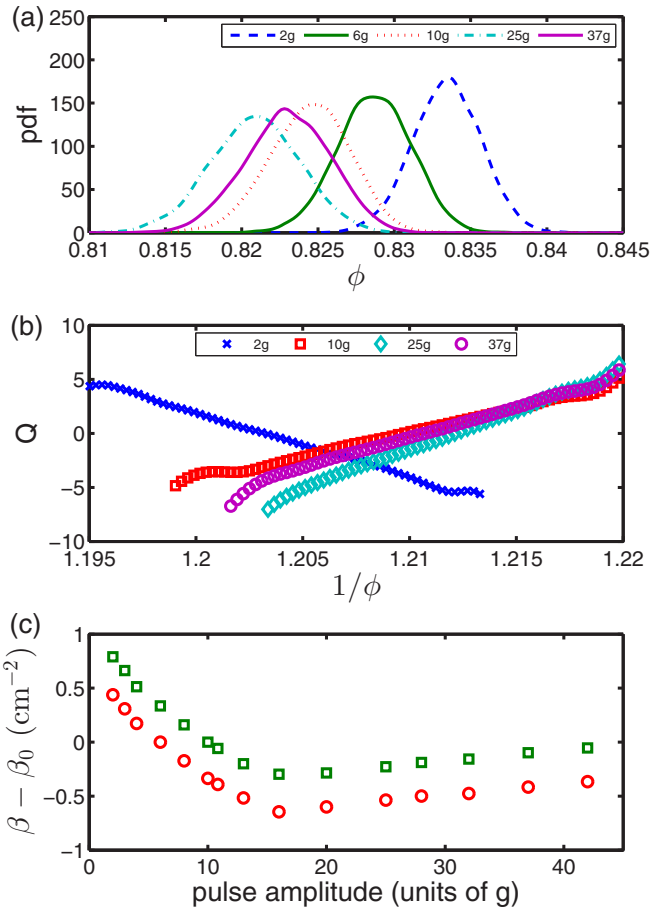

FIG. 7. (Color online) (a) Probability density function of the volume fraction for the "negative-g" protocol, estimated with the kernel density method, for different values of the pulse strength. (b) The quantity Q from Eq. (20) for some values of the tapping parameter, where the distribution with $g_p = 6$ was chosen as denominator in Eq. (19). (c) The compactivity calculated with the help of the overlapping histogram method using the distribution with $g_p = 6$ (green squares) and $g_p = 10$ (red circles) as denominator in Eq. (19).

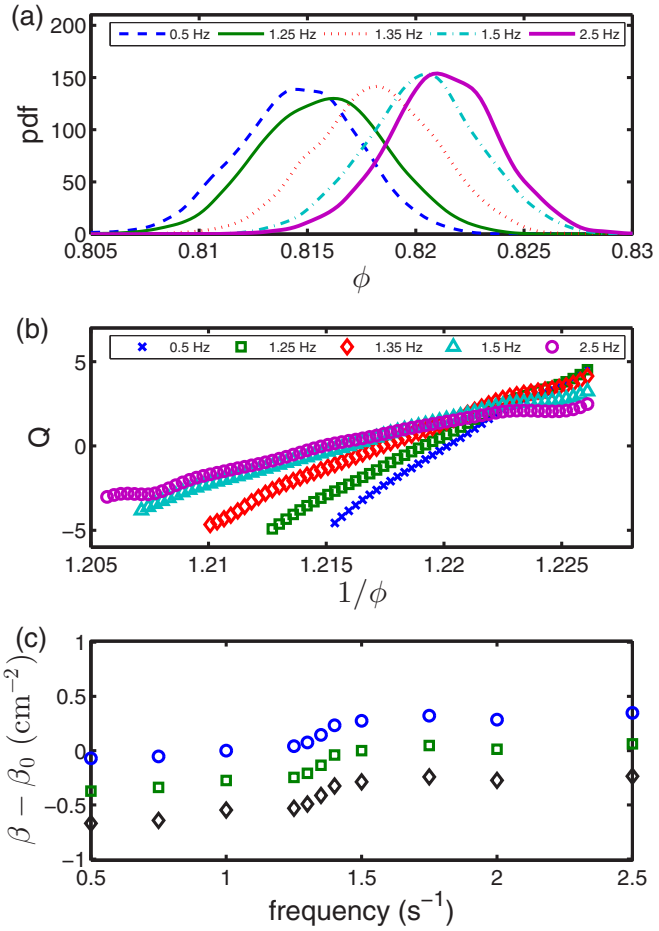

FIG. 8. (Color online) (a) Probability density function of the volume fraction for samples of the "rotating-g" protocol, estimated with the kernel density method, for different values of the rotation frequency. (b) The quantity Q from Eq. (20) for some values of the tapping parameter using the distribution with $g_p = 6$ of the "negative-g" protocol as denominator in Eq. (19). (c) The compactivity calculated with the help of the overlapping histogram method using the distribution from the "rotating-g" protocol with $f = 0.5$ Hz (blue circles), $f = 1.25$ Hz (green squares) and the distribution from the "negative-g" protocol with $g_p = 6$ (black diamonds) as denominator.

the distributions are Gaussian, we used a chi-square test [49] with a significance level of 5%. The null hypothesis that the data is normally distributed was rejected for all samples [56]. Although Gaussians may still be good approximations to the central region of our distributions, we take this as evidence for a statistical mechanical origin of these distributions rather than their emergence from some unknown additive process not related to phase-space exploration. Therefore, we believe that our data do not give spurious results due to the pitfall described in Appendix A.

We also show in Appendix A that while the presence of Gaussian distributions may lead to false positive results regarding the validity of Edwards's theory [27], this is by no means true for all Gaussian distributions: In the limit of large numbers, the canonical distribution corresponding to a fixed compactivity must become Gaussian as well, and this distribution obviously satisfies Edwards's theory by definition. We take the fact that the tails of our distributions are non-Gaussian together with the verification of (20) as an indication that the theory works. This interpretation is supported by other studies of very similar systems where the volume-per-particle distribution (which is not a sum and therefore not subject to the central limit theorem) was found not to be Gaussian [17,27] even in the central region.

In terms of volume fraction, equation (20) reads:

$$Q = \ln \frac{P(\phi,\beta_1)}{P(\phi,\beta_0)} = -(\beta_1 - \beta_0)\frac{V_g}{\phi} - \ln \frac{Z(\beta_1)}{Z(\beta_0)}. \qquad (39)$$

We note that (39) is interpreted in terms of a canonical ensemble, which implies the number of particles to be a constant. This means that the total volume of the grains V_g in the test volume must be a constant [57]. In principle, one would have to adapt the test volume size V_T used in determining the volume fraction distribution to the measured mean volume fraction $\bar{\phi}$ in such a way that $V_g = V_T\,\bar{\phi}$ remains constant. The size of the test volume would then be a function of the mean volume fraction. This could become important, if very

small test volumes were used. The standard deviation of the volume fraction distribution should decrease with increasing test volume as $\sigma \propto V_T^{-1/2}$, which follows from (17), while $\bar{\phi}$ does not depend on the system size. By using a constant test volume V_T, the magnitude of differences in V_g due to different volume fractions is bounded by $\Delta V_g = V_T(1/\phi_{\mathrm{rcp}} - 1/\phi_{\mathrm{rlp}}) \simeq 0.05 V_T$. If the test volume is large compared to the size of the particles, the relative error which is made by using a constant test volume, assuming that the cumulative grain volume is constant (in spite of the different volume fractions), corresponds to approximately 2–3%. This is smaller than the confidence interval of σ_ϕ due to the finite sample size and therefore negligible.

By choosing a reference probability distribution which is used as the denominator in Eq. (39) we are able to determine the inverse compactivity and the logarithm of the partition function up to additive constants, which are the unknown inverse compactivity of the reference distribution and the unknown logarithm of the partition function thereof, respectively. In order to avoid errors due to insufficient data in the tails of the distribution, we evaluated the slope of Q only in regions where the value of each distribution involved in the calculation of (39) is bigger than 5% of its maximum.

Figures 7(b) and 8(b) show the quantity Q for some samples as function of the inverse volume fraction, where the distribution with $g_p = 6$ of the "negative-g" protocol was chosen as the reference distribution, because it has sufficient overlap with all the other distributions. We tried several other distributions as references, too. So long as the distribution overlap was big enough, we always found a linear relation between Q and the inverse volume fraction ϕ^{-1}. This may be interpreted as suggestive of the validity of Edwards's assumptions. Note that the deviations from the straight line on the left and right ends of the curves are due to insufficient number of sampling data points in that region. Therefore the estimated probability density function behaves like the tails of the sampling kernel, which is reflected also in Q. This behavior is a mathematical artifact and not a systematic deviation from a straight line.

From (39), it follows immediately that the values determined for β using different samples as reference distribution may only differ by an additive constant. This prediction holds for the "negative-g" protocol as is demonstrated in Fig. 7(c). There the samples with $g_p = 6$ and $g_p = 10$ were used as reference distributions. The same is true for the "rotating-g" protocol [Fig. 8(c)] when we used samples corresponding to different values of the rotating frequency. It even applies if we use samples from the "negative-g" protocol as reference distribution, in agreement with the fact that the predictions of Edwards's theory should be protocol independent.

From now on, we use the distribution from the "negative-g" protocol with $g_p = 6$ as reference distribution for all the following calculations. Figure 9 shows the values determined for the inverse compactivity for both protocols as function of the volume fraction. All the data, whether obtained from the branch left of the minimum or the branch right of the minimum in the $\phi(g_p)$ curve of the "negative-g" protocol (cf. Fig. 5) or else from the "rotating-g" protocol is fitted by the same function $\beta(\phi)$. This is a strong indicator for the applicability of Edwards's theory to our samples.

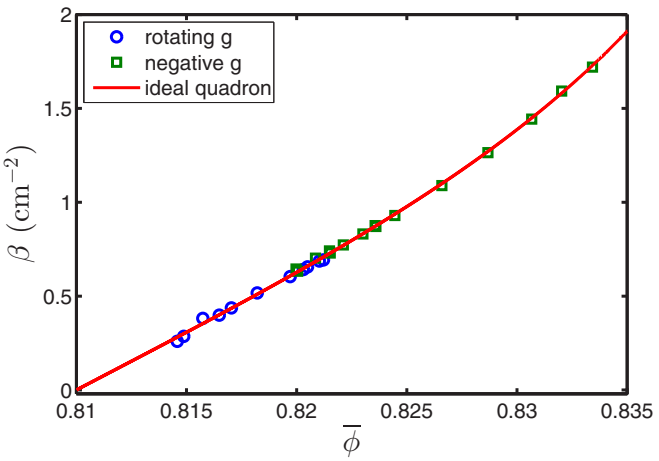

FIG. 9. (Color online) The compactivity as function of the volume fraction density for the "negative-g" protocol (square) and for the "rotating-g" protocol (diamonds). The values were corrected with the additive constant β_0 determined from the ideal quadron fit. The solid line is a fit to the ideal quadron solution (26).

In order to fit our results to an analytical function, we used the ideal quadron solution (26). The values of random loose packing (rlp) and random close packing (rcp) were assumed to be $\phi_{\mathrm{rlp}} = 0.81$ and $\phi_{\mathrm{rcp}} = 0.855$. The choice of these values was pragmatic. To our knowledge, there are no studies about the exact values for random close and random loose packing for bidisperse decagons. Furthermore, the values of rlp and rcp will depend on on the size ratio between the particles. Therefore, we used plausible values obtained for (bidisperse) disks [17,58,59]. We checked that the influence of the values of random loose and random close packings on the values of the obtained parameters are smaller than 20%, as long as the values are in the plausible interval.

$N\bar{z}/V_g$ was used as fitting parameter. Since we can determine the inverse compactivity only up to an additive constant from the overlapping histogram method, we made the replacement $\beta \to \tilde{\beta} + \beta_0$ in Eq. (26), where $\tilde{\beta}$ is the value determined from the simulations and β_0 is taken as an additional fit parameter. Note that the determination of β_0 is possible as we assumed that the inverse compactivity is fixed at random loose and random close packing and that this is not specific to the ideal quadron fit. We emphasize that the parameter β_0 only shifts the whole curve shown in Fig. 9 upward or downward and is the same for both protocols. Since the *same* value of β_0 was added to *every* data point obtained from the overlapping histogram method for the comparison of the fit function with the simulation data in Fig. 9, this value does not influence the conclusion that the compactivity is the same for both protocols. The fit describes the simulation data very well, as is seen in Fig. 9. However, we find as fitting value $N\bar{z}/V_g = 556.51\ \mathrm{m}^{-2}$, which differs by about a factor of 40 from the values used in the simulation. This might be understood by assuming that approximately 40 quadrons constitute a statistically independent unit in the granular ensemble. This issue certainly needs further study. We also tried to fit ϕ_{rlp} and ϕ_{rcp} using the known particle number in Eq. (26) but this leads to an unphysical value for random close packing of about $\phi_{\mathrm{rcp}} \simeq 1.2$.

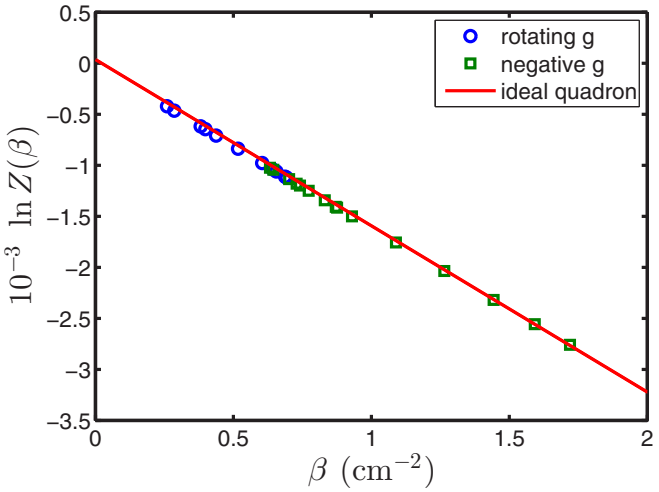

FIG. 10. (Color online) The logarithm of the partition function, determined from the overlapping histogram method (symbols). The solid line is the ideal quadron solution.

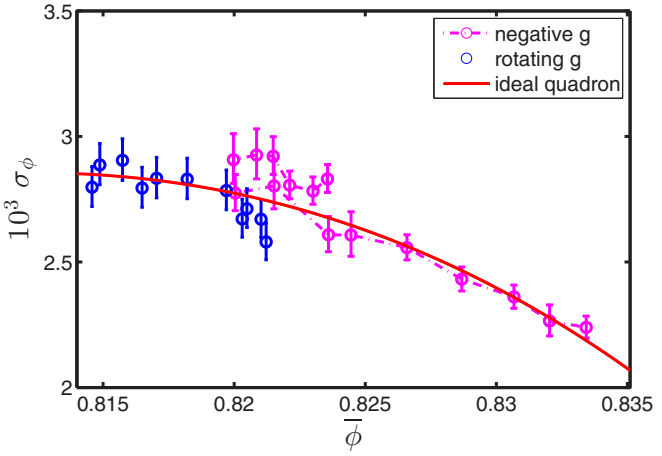

FIG. 11. (Color online) The volume fraction fluctuation (standard deviation) as function of the mean volume fraction. The blue points correspond to the "rotating-g" protocol and the magenta points and lines corresponds to the negative-g" protocol. The solid line is the ideal quadron fit.

When we used only the data obtained by one of the protocols to determine the parameters of the ideal quadron solution, the solution fitted the data of the other protocol. The relative deviation of the obtained fitting parameters is smaller the 2%. Because this results in curves that are indistinguishable to the eye, only the fit using the whole data set is presented in Fig. 9. Nevertheless, this means that we can predict the $\beta(\phi)$ curve, for the "rotating-g" protocol using the data determined from the "negative-g" protocol and vice versa. However, for all compactivities determined, the same *reference* distribution was used so the data of the fit employed for the one and the other protocol was not entirely independent.

While the slope of Q allows us to determine the inverse compactivity, the axis intercept B determines the logarithm of the partition function

$$B = -\ln Z(\beta) + \ln Z(\beta_0). \tag{40}$$

If the assumptions leading to (39) are correct, the partition function of the ideal quadron solution (21) should describe the found intercept without additional fitting. The parameters Δ, V_0, Nz are directly related to the parameters determined via Eqs. (24) and (25). As Fig. 10 shows, the numerically determined values and the ideal quadron solution fit very well, independently of the protocol and of the branch in the "negative-g" protocol.

Using (26) in Eq. (17), we get the relationship between the mean volume fraction and its fluctuations. The result together with simulation data obtained directly is shown in Fig. 11. The data is in good agreement with the theory for both protocols.

We mention that in a former study which used vertically tapped monodisperse regular polygons [60], a maximum in the ϕ-σ curve was reported which coincided with an inflexion point in the impulse strength-volume fraction curve. In our simulation we do not see this effect, also in experimental work about bidisperse two dimensional systems such a maximum was not observed [17]. It might be suspected that crystallization effects that occur frequently in two-dimensional monodisperse systems were responsible for the occurrence of the maximum in Ref. [60], but this is a speculation, given that the simulation was done with decagons, not normally expected to crystallize.

However, we cannot exclude that there may be a small hysteresis for the branch pieces to the left of minimum and to the right of minimum, respectively (cf. Fig. 5). Clearly, if the volume ensemble completely described all structural degrees of freedom and the probability distribution, two states with the same β and the same ϕ would be identical and therefore σ_ϕ would also have to be the same. However, if the volume ensemble is only a good approximation of the geometric aspects of interdependent force-moment and volume ensembles (see, e.g., Ref. [6]), deviations may occur.

VI. LIMITATIONS OF THE VOLUME ENSEMBLE

Whereas the volume ensemble appears to succeed in describing the geometrical and structural degrees of freedom of a granular aggregate, this is not the case for the stress state of the latter. If the volume ensemble entailed a complete description of a granular state and its probability distribution, then the mean stress of the system would have to be a unique function of the inverse compactivity and therefore also a unique function of the mean volume fraction. We computed the mean extensive stress (or force-moment tensor), defined as

$$\boldsymbol{S}_{ij} = \sum_p V^p \sigma_{ij}^p \tag{41}$$

as a function of the volume fraction. Note that the volume density of this tensor is the stress itself. Here i and j label Cartesian coordinates. The sum runs over all particles, where σ_{ij}^p is the mean stress in particle p and V^p is the volume associated with the particle. The result is shown in Fig. 12. The stress tensor is obviously not a unique function of the volume fraction.

Neither the results from the different protocols nor the results from the half-branches left to the minimum and right to the minimum, respectively, of the "negative-g" protocol

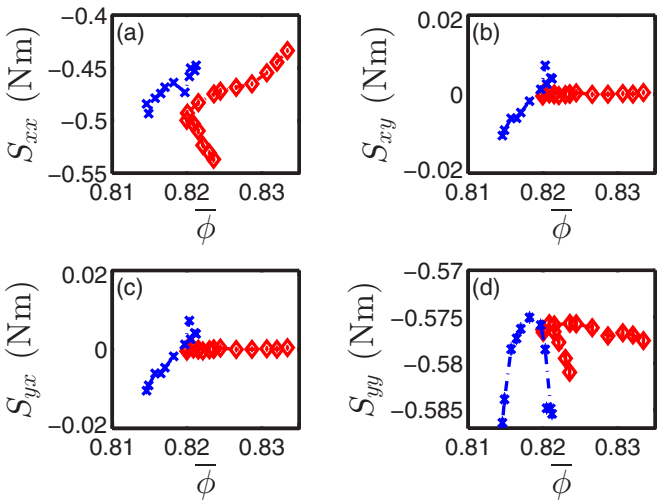

FIG. 12. (Color online) The components of the extensive stress tensor as function of the mean volume fraction for the "negative-g" protocol (diamonds) and the "rotating-g" protocol (crosses).

fall on the same curve, which is in agreement with similar findings on tapped granular matter [52]. Two systems with almost identical particle positions and orientations can be in very different stress states which is not captured by the volume ensemble. To describe the stress state and the volume state together, probably the combined volume-stress ensemble [6] must be taken into account. We remark that it is unclear so far whether the stress states observed here are "very different" or even "very similar" because we do not know the size of the accessible phase space for the extensive stress tensor. Maybe the deviations in our systems which have magnitude on the order of 0.01 Nm are so small that it is reasonable to assume in first approximation that the stress-moment tensor is almost constant which would be a possible explanation for the success of assuming a pure volume ensemble.

VII. CONCLUSIONS

We used two different protocols to excite a granular ensemble periodically. The inverse compactivity was determined as a function of the mean volume fraction and we found that the relation between the compactivity and the mean volume fraction is protocol independent. We determined an expression for the logarithm of the partition function and thus the thermodynamic potential which is the equivalent of the free energy of classical statistics. This was done by using the ideal quadron solution derived by Blumenfeld and Edwards [29] as a fitting function. Even though the ideal quadron solution makes very rough assumptions, the resulting description is in qualitative agreement with the findings from the simulations. If the particle number is used as a fit parameter instead of calculating the distribution with the true particle number, then the ideal quadron solution is also able to describe the results quantitatively.

We found that all our simulation results related to structural quantities are compatible with Edwards's theory and that the Edwards theory describes the volume fluctuations very well, independently of the excitation protocol. The usage of the Edwards volume ensemble seems to be sufficient for the description of system properties which are related to the geometrical arrangement of the grains, but, as might be expected from previous findings, it is not sufficient to describe the stress states of the granular ensemble.

APPENDIX A: OVERLAPPING HISTOGRAMS FOR GAUSSIAN DISTRIBUTIONS

If two volume samples were Gaussian distributed with mean values V_1 and V_2 and variances σ_1^2 and σ_2^2, the corresponding Q function defined in Eq. (19) would be [27]:

$$Q^g(V) = -\frac{(V-V_1)^2}{2\sigma_1^2} + \frac{(V-V_2)^2}{2\sigma_2^2} + \ln\left(\frac{\sigma_2}{\sigma_1}\right). \tag{A1}$$

This is a quadratic function of V, but in some V interval the curvature of Q^g may be very small and the parabolic function (A1) would then practically be indistinguishable from a linear function. This happens in particular if the variances σ_1 and σ_2 are close to each other, i.e., for nearby compactivities. If we define a function A_{21}^g as the slope of (A1) midway between the maximum values of the two normal distributions,

$$A_{21}^g := \frac{d}{dV} Q^g(V)\Big|_{V=(V_1+V_2)/2}, \tag{A2}$$

then we obtain [27]:

$$A_{21}^g = \frac{1}{2}\left(\frac{1}{\sigma_1^2} + \frac{1}{\sigma_2^2}\right)(V_1 - V_2). \tag{A3}$$

Identifying formally

$$A_{21}^g = \beta(V_2) - \beta(V_1), \tag{A4}$$

we find from (A3):

$$-\frac{V_2 - V_1}{\beta(V_2) - \beta(V_1)} = 2\left(\frac{1}{\sigma_1^2} + \frac{1}{\sigma_2^2}\right)^{-1}. \tag{A5}$$

If we assume that the variance is a unique function of the mean volume, then this equation is an approximation of (12) which is the better the smaller the difference $|V_2 - V_1|$.

We note that the formal identification (A4) is, strictly speaking, inherently contradictory, which is easy to see if we calculate Q for a third sample with mean value V_3 and variance σ_3 and the same reference sample in the denominator. From (A4) $A_{31} - A_{21} = A_{32}$ follows, but if one calculates the same quantity from (A3), then the result does not agree. (However, the identification is possible if the three variances are the same.)

Analogously, we can calculate the intercept B_{21}^g of the tangent which touches (A1) at $V = (V1 + V2)/2$:

$$B_{21}^g = \frac{1}{8}(V_2 - V_1)^2\left(\frac{1}{\sigma_2^2} - \frac{1}{\sigma_1^2}\right) + \ln\left(\frac{\sigma_2}{\sigma_1}\right) + \frac{1}{4}\left(V_2^2 - V_1^2\right)\left(\frac{1}{\sigma_1^2} + \frac{1}{\sigma_2^2}\right). \tag{A6}$$

By calculating the limit

$$\lim_{V_2 \to V_1} \frac{B_{21}^g}{A_{21}^g} = -V_1 - \sigma_1 \frac{\partial \sigma_1}{\partial V_1} \tag{A7}$$

we find that the term B_{21}^g/A_{21}^g is an approximation for (10) if we assume $\frac{\partial\sigma_1}{\partial V_1}$ to be negligibly small and formally identify $B_{21}^g = \ln(Z_2) - \ln(Z_1)$. Again the approximation becomes better as the difference between the volume V_2 and the reference volume V_1 gets smaller.

Due to these similarities, it might occur, even if the relations (10), (12), and (20) are consistent, that within the limits of data precision it is not possible to decide whether the reason of this agreement is the correctness of Edwards's theory or the fact that the data generated by a specific protocol happen to have a distribution that is well approximated by a normal distribution. If the samples are generated using the same protocol, then one may expect that there is a function $\sigma(V)$, but when different protocols are used, it would be surprising if both protocols led to the same relation, unless a general principle, such as Edwards's theory, were at work.

On one hand, these similarities make it more difficult to verify Edwards's theory. On the other hand, due to the central limit theorem, we should expect that the distribution of Eq. (18) becomes more and more Gaussian with increasing system size. Therefore, it is not always true that the appearance of Gaussian distributions signifies inapplicability of the overlapping histogram method in the determination of the compactivity and of related quantities. Let us briefly have a look at this. Rewriting Eq. (18) for general β and using the microcanonical result for the density of states, we have

$$P(V,\beta,N) = \frac{\Omega(V,N)}{Z(\beta,N)} e^{-\beta V} = \frac{e^{S(V,N)-\beta V}}{Z(\beta,N)}. \tag{A8}$$

As in standard statistical mechanics, we can then argue that for *large* systems this distribution has a sharp peak at the mean value of the volume and we may expand the entropy about this average, neglecting terms that are of higher than quadratic order:

$$S(V,N) - \beta V \approx S(\bar{V},N) + \beta(\bar{V})\big(V-\bar{V}\big) + \frac{1}{2}\frac{\partial^2 S}{\partial V^2}\bigg|_{\bar{V}} \big(V-\bar{V}\big)^2 - \beta V. \tag{A9}$$

In order for the expansion to be about the maximum of the distribution, we must require the linear order term to vanish, i.e., we have $\beta(\bar{V}) = \beta$, meaning equivalence of the microcanonical and the canonical compactivity definitions. Identifying the inverse of $-\partial^2 S/\partial V^2$ with the variance, our distribution takes the form

$$P(V,\beta,N) = \frac{e^{S(\bar{V},N)-\beta\bar{V}-\left(V-\bar{V}\right)^2/2\sigma^2}}{Z(\beta,N)}. \tag{A10}$$

Evaluating this at two different compactivities and taking the logarithm of the ratio, we find (denoting the mean volumes by V_1 and V_2 again)

$$\begin{aligned} Q(V) &= \ln\frac{P(V,\beta_1,N)}{P(V,\beta_2,N)} \\ &= -\frac{(V-V_1)^2}{2\sigma_1^2} + \frac{(V-V_2)^2}{2\sigma_2^2} - \beta_1 V_1 + S(V_1,N) \\ &\quad + \beta_2 V_2 - S(V_2,N) + \ln\frac{Z(\beta_2,N)}{Z(\beta_1,N)}, \end{aligned} \tag{A11}$$

which is nothing but (A1) with an explicit expression for $\ln(\sigma_2/\sigma_1)$. But we have derived this as an approximation to the distribution (18) from which we obtain Eq. (20) for Q. If we substitute β_2 for β_0 in that equation, then we see that the following (nontrivial) approximation holds in sufficiently large systems (close to the "thermodynamic limit"), as long as the distributions overlap significantly (which of course becomes less likely with increasing system size):

$$\begin{aligned} -(\beta_1-\beta_2)V \approx &-\frac{(V-V_1)^2}{2\sigma_1^2} + \frac{(V-V_2)^2}{2\sigma_2^2} \\ &- \beta_1 V_1 + S(V_1,N) + \beta_2 V_2 - S(V_2,N). \end{aligned} \tag{A12}$$

Hence, the sum on the right-hand side that is quadratic in V is a good approximation to the sum on the left-hand side that is linear in V. As we have shown by this small calculation, the overlapping-histogram method will give, for such a system, the correct linear dependence on V, despite the fact that the central part of the distribution is well approximated by a Gaussian. In simulations, this behavior might be distinguished from Gaussian distributions not having the statistical mechanical origin postulated by the Edwards theory through verification that the tails of the simulated distributions, i.e., their behavior for V values, where the quadratic approximation (A9) breaks down, are not Gaussian. This was done for our simulations via the chi-square test mentioned in Sec. V.

APPENDIX B: KERNEL DENSITY ESTIMATION

A method to determine a continuous probability density from a data sample is the kernel density estimation method (KDE) [53,54]. If $x_1, x_2, \ldots, x_n$ are sampled data, the kernel density estimation of the probability density $P(x)$ at the point x is defined as

$$P(x) = \frac{1}{nh}\sum_{i=1}^{n} K\left(\frac{x-x_i}{h}\right), \tag{B1}$$

where $K(x)$ is the kernel which must be a non-negative function that satisfies

$$\int_{-\infty}^{\infty} dx\, K(x) = 1 \tag{B2}$$

and h is a smoothing parameter called the bandwidth. Possible kernels are, for example, the normal kernel

$$K(x) = \frac{1}{2\pi}\exp(-x^2/2), \tag{B3}$$

the Cauchy kernel

$$K = \frac{1}{\pi(1+x^2)}, \tag{B4}$$

the Epanechnikov kernel

$$K(t) = \begin{cases} \frac{3}{4}(1-x^2) & \text{if } x \in [-1;1] \\ 0 & \text{elsewhere} \end{cases}, \tag{B5}$$

or even the rectangular kernel:

$$K(t) = \begin{cases} 1 & \text{if } x \in [-1/2;1/2] \\ 0 & \text{elsewhere} \end{cases}. \tag{B6}$$

The latter is equivalent to a histogram with bin width h. While it can be shown that the Epanechnikov kernel is optimal in the sense that it minimizes the mean-squared error between the estimated and the real probability distributions, we used a normal kernel since it allows us to make a good estimation of the optimal bandwidth h. In general, the optimal bandwidth can only be calculated if one knows the underlying probability density, but this density is unknown. In practice, therefore, Silverman's rule of thumb is often used. Under the assumption that the underlying probability distribution is Gaussian and if a Gaussian kernel is used, the optimal bandwidth is

$$\left(\frac{4\sigma^5}{3n}\right)^{\frac{1}{5}} \simeq 1.06\sigma n^{-1/5}, \tag{B7}$$

where σ is the standard derivation of the sample. It turns out that this bandwidth is also a reasonable choice in practical situations, if the underlying distribution is not Gaussian. We note that for small data sets the choice of the kernel may have a significant influence on the quality of the fit. However, if the data sample becomes big enough, all kernels lead to almost the same results except for the far tail of the distribution, where no data points are available. In this region, the kernel itself specifies the decay of the distribution. As it is shown exemplarily in Fig. 13, the choice of the kernel is not crucial for our data samples. The results obtained with the optimal Epanechnikov Kernel and those achieved with the normal kernel are practically indistinguishable. The box kernel which is equivalent to a shifted histogram is a little bit more more irregular. We preferred the normal kernel, in order to avoid an *ad hoc* choice of the kernel bandwidth.

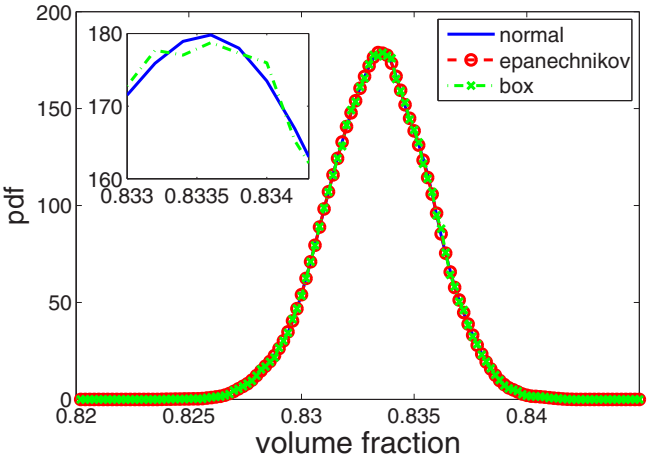

FIG. 13. (Color online) Comparison of the results of kernel density estimation using different kernels. The shown data were obtained from the volume fraction time series of the "negative-g" protocol with the tapping parameter $g_p = 8$, for other parameters we found the same conclusion. The results due to the Epanechnikov kernel and the normal kernel are indistinguishable, the box kernel results in a little bit more irregular estimations. The inset shows the normal and the box kernel in the central region of the distribution.

[1] S. F. Edwards and R. Oakeshott, Physica A **157**, 1080 (1989).
[2] S. F. Edwards and R. Oakeshott, Physica D **38**, 88 (1989).
[3] D. P. Bi, S. Henkes, K. E. Daniels, and B. Chakraborty, Annu. Rev. Condensed Matter Phys. **6**, 63 (2015).
[4] S. Henkes, C. S. O'Hern, and B. Chakraborty, Phys. Rev. Lett. **99**, 038002 (2007).
[5] R. Blumenfeld and S. F. Edwards, Eur. Phys. J. E **19**, 23 (2006).
[6] R. Blumenfeld, J. F. Jordan, and S. F. Edwards, Phys. Rev. Lett. **109**, 238001 (2012).
[7] R. Blumenfeld and S. F. Edwards, Eur. Phys. J. Spec. Top. **223**, 2189 (2014).
[8] J. G. Puckett and K. E. Daniels, Phys. Rev. Lett. **110**, 058001 (2013).
[9] If we assume exchange of the volume associated with a particle to be restricted between the two particle types, an incomplete "equilibrium" with different compactivities might arise. A thermodynamic analog would be the fountain effect, where two receptacles with superfluid helium are connected by a supercapillary, allowing only particle exchange of the superfluid component but no energy exchange. Due to the restricted energy exchange, equilibrium configurations with different temperatures (and pressures) in the two containers exist. Alternatively, it is possible that this was a protocol related effect or even a finite-size effect, because the subsystem consisted of 100 particles only.
[10] E. R. Nowak, J. B. Knight, E. Ben-Naim, H. M. Jaeger, and S. R. Nagel, Phys. Rev. E **57**, 1971 (1998).
[11] J. C. Tsai, G. A. Voth, and J. P. Gollub, Phys. Rev. Lett. **91**, 064301 (2003).
[12] M. Pica Ciamarra, A. Coniglio, and M. Nicodemi, Phys. Rev. Lett. **97**, 158001 (2006).
[13] F. Paillusson and D. Frenkel, Phys. Rev. Lett. **109**, 208001 (2012).
[14] L. A. Pugnaloni, M. Mizrahi, C. M. Carlevaro, and F. Vericat, Phys. Rev. E **78**, 051305 (2008).
[15] M. Schröter, D. I. Goldman, and H. L. Swinney, Phys. Rev. E **71**, 030301 (2005).
[16] J. Zhao, S. Sidle, H. Swinney, and M. Schroeter, Europhys. Lett. **97**, 34004 (2012).
[17] S.-C. Zhao and M. Schröter, Soft Matter **10**, 4208 (2014).
[18] F. Paillusson, Phys. Rev. E **91**, 012204 (2015).
[19] D. Asenjo, F. Paillusson, and D. Frenkel, Phys. Rev. Lett. **112**, 098002 (2014).
[20] L. D. Landau and E. M. F. Lifschitz, *Lehrbuch der theoretischen Physik* (Akademie-Verlag, Berlin, 1987).
[21] F. Lechenault, F. d. Cruz, O. Dauchot, and E. Bertin, J. Stat. Mech.: Theor. Exp. (2006) P07009.
[22] R. K. Bowles and S. S. Ashwin, Phys. Rev. E **83**, 031302 (2011).
[23] R. Irastorza, C. M. Carlevaro, and L. A. Pugnaloni, J. Stat. Mech.: Theor. Exp. (2013) P12012.
[24] A. Nourmohammad, T. Held, and M. Laessig, Curr. Opin. Genet. Dev. **23**, 684 (2013).
[25] N. H. Barton and J. B. Coe, J. Theor. Biol. **259**, 317 (2009).
[26] D. S. Dean and A. Lefevre, Phys. Rev. Lett. **90**, 198301 (2003).
[27] S. McNamara, P. Richard, S. K. de Richter, G. Le Caer, and R. Delannay, Phys. Rev. E **80**, 031301 (2009).
[28] M. P. Ciamarra, P. Richard, M. Schröter, and B. P. Tighe, Soft Matter **8**, 9731 (2012).

[29] R. Blumenfeld and S. F. Edwards, Phys. Rev. Lett. **90**, 114303 (2003).
[30] T. Aste and T. D. Matteo, Eur. Phys. J. B **64**, 511 (2008).
[31] G. Voronoi, J. Reine Angew. Math. **134**, 198 (1908).
[32] B. Delaunay, Bull. Acad. Sci. USSR **6**, 793 (1934).
[33] T. Aste, T. D. Matteo, M. Saadatfar, T. J. Senden, M. Schröter, and H. L. Swinney, Europhys. Lett. **79**, 24003 (2007).
[34] D. Slobinsky and L. A. Pugnaloni, J. Stat. Mech.: Theor. Exp. (2015) P02005.
[35] R. C. Ball and R. Blumenfeld, Phys. Rev. Lett. **88**, 115505 (2002).
[36] M. P. Ciamarra, Phys. Rev. Lett. **99**, 089401 (2007).
[37] R. Blumenfeld and S. F. Edwards, Phys. Rev. Lett. **99**, 089402 (2007).
[38] M. P. Ciamarra and A. Coniglio, Phys. Rev. Lett. **101**, 128001 (2008).
[39] A. Schinner, Granular Matter **2**, 35 (1999).
[40] A. Schinner, Ein Simulationssystem für granulare Aufschüttungen aus Teilchen variabler Form, Ph.D. thesis, University of Magdeburg, 2001.
[41] P. Roul, A. Schinner, and K. Kassner, Granul. Matter **13**, 303 (2011).
[42] P. Roul, A. Schinner, and K. Kassner, Powder Technol. **214**, 406 (2011).
[43] P. Roul, A. Schinner, and K. Kassner, Geotech. Geol. Eng. **29**, 597 (2011).
[44] M. C. Lin, Efficient collision detection for animation and robotics, Ph.D. thesis, University of California at Berkeley, 1993.
[45] T. Schwager and T. Poeschel, Granul. Matter **9**, 465 (2007).
[46] P. A. Cundall and O. D. L. Strack, Geotechnique **29**, 47 (1979).
[47] C. W. Gear, Math. Comp. **21**, 146 (1967).
[48] I. G. Tejada and R. Jimenez, Eur. Phys. J. E **37**, 15 (2014).
[49] I. Bronstein, Semendjajew, G. K.A. Musiol, and H. Mühlig, *Taschenbuch der Mathematik* (Harri Deutsch Verlag, Frankfurt am Main, 1999).
[50] P. A. Gago, D. Maza, and L. A. Pugnaloni, Phys. Rev. E **91**, 032207 (2015).
[51] P. A. Gago, N. E. Bueno, and L. A. Pugnaloni, Granul. Matter **11**, 365 (2009).
[52] L. A. Pugnaloni, I. Sanchez, P. A. Gago, J. Damas, I. Zuriguel, and D. Maza, Phys. Rev. E **82**, 050301 (2010).
[53] M. Rosenblatt, Ann. Math. Statist. **27**, 832 (1956).
[54] E. Parzen, Ann. Math. Statist. **33**, 1065 (1962).
[55] B. Silverman, *Density Estimation for Statistics and Data Analysis* (Chapman & Hall/CRC, London, 1998).
[56] Note that in early test simulations with approximately 100 taps, the null hypothesis was not rejected, and one needs enough data to decide about this hypothesis.
[57] Equation (20) could be interpreted as describing a grand-canonical ensemble as well and would be evaluable for variable particle number. With (39) this is problematic, because then the compactivity would be multiplied by two factors V_g and ϕ that might both vary.
[58] J. G. Berryman, Phys. Rev. A **27**, 1053 (1983).
[59] L. E. Silbert, Soft Matter **6**, 2918 (2010).
[60] C. M. Carlevaro and L. A. Pugnaloni, J. Stat. Mech.: Theor. Exp. (2011) P01007.